NANO LETTERS

pubs.acs.org/NanoLett Letter

Monolayer MoS_2 Sensors for Probing the Self-Heating Effect in Indium Tin Oxide Nanoelectronics

Neil Ghosh, Zehao Lin, Monoranjan Debnath Rony, Sahej Sharma, Jian-Yu Lin, Zheng Sun, Zhihong Chen, Joerg Appenzeller, Thomas E. Beechem, Peide D. Ye,* and Xianfan Xu*

Cite This: https://doi.org/10.1021/acs.nanolett.5c05421 Read Online

ACCESS | Metrics & More | Article Recommendations | Supporting Information

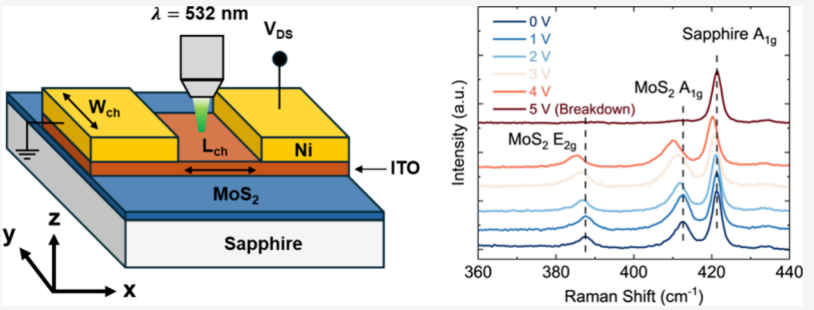

ABSTRACT: Amorphous oxide semiconductors such as indium tin oxide (ITO) are promising channel materials for back-end-of-line memory and logic devices, yet their performance and reliability are hindered by self-heating at high power densities. Precise quantification of channel temperature and heat dissipation pathways into the surrounding materials is therefore essential for effective thermal management and the 3D heterogeneous integration of these devices. This work investigates heat dissipation in ultrathin ITO devices on sapphire by Raman thermometry, using an interfacial monolayer of MoS_2 as an in situ temperature sensor. Thermal boundary resistance of each interface in the device is independently measured by time-domain thermoreflectance and then used in finite-element simulations of device temperatures, thereby decoupling temperature measurements from interface characterization. Simulated temperatures incorporating measured electrical and thermal characteristics corroborate well with Raman thermometry. Our validated framework highlights the central role of interfacial resistance and heat spreading through the substrate on heat dissipation in thin-film nanoelectronics.

KEYWORDS: *Raman thermometry, thermal boundary resistance, self-heating effect, oxide semiconductor, high-field breakdown, molybdenum disulfide*

Thin-film amorphous oxide semiconductors have attracted significant attention as promising channel materials for back-end-of-line (BEOL)-compatible logic and memory devices.[1−4] Recently, indium tin oxide (ITO) has stood out as a particularly attractive candidate due to properties such as low thermal budget for large-scale fabrication, high on-current, and low leakage.[5−7] Despite this progress, a critical challenge that remains underexplored in ITO devices is the mitigation of the self-heating effect (SHE), which can limit performance and long-term device reliability at high power densities (PDs).[7−9] These issues are likely to be exacerbated during the possible 3D heterogeneous integration of these devices, where amorphous oxide channels are also being explored as BEOL voltage converters[10,11] and high-current RF devices,[12,13] both of which can experience strong SHE, as the heat dissipation pathways into the surrounding materials are usually limited by the poor heat transfer across interfaces. Consequently, thermal interface and substrate design often become a bottleneck rather than the intrinsic electronic properties of the amorphous oxide channel. Hence, to adequately address these thermal management challenges, precise measurements of the ITO channel temperature and the quantification of its surrounding thermal interfaces are a crucial task.

Su et al.[9] recently investigated Al_2O_3-capped ITO devices using scanning thermal microscopy (SThM), while thermal studies on other oxide semiconductors have utilized techniques such as thermoreflectance imaging[14−17] and infrared thermography[18] to probe the temperature rise in the device channel due to SHE. The thermal boundary resistance (TBR) of the surrounding interfaces is then usually estimated from the channel temperature using a simplified thermal resistor network or finite-element simulations and matched against

Received: October 29, 2025
Revised: March 8, 2026
Accepted: April 3, 2026

values reported in the literature. However, this indirect approach limits the ability to independently validate the temperature measurements since the extracted TBR is inherently dependent on the measured temperature. This highlights the importance of developing alternative methodologies that can decouple the thermometry from the interface property characterization, enabling a more reliable and independent assessment of device thermal behavior.

Raman spectroscopy has been widely used as a noncontact method to quantify temperature,[19−21] strain,[20,22−24] and doping,[24−27] as well as to extract properties such as in-plane thermal conductivity[28−33] of ultrathin materials. This technique is particularly useful in analyzing thermal transport across heterogeneous device stacks, as the distinct signatures of different Raman-active layers can be used to simultaneously acquire their temperatures. Several studies have further used the device temperature acquired by Raman thermometry to estimate TBR.[19,34−37] However, it is important to note that when the heating of the Raman-active material is primarily provided by the Raman laser itself, the extracted TBR tends to be an overestimation, as the phonons excited by optical heating inside the channel can be out of thermal equilibrium with phonons responsible for carrying heat across the interfaces, creating an additional internal thermal resistance.[36,38,39] In contrast, in device configurations where the dominant heating mechanism of the Raman-active layer is external electrical heating, all relevant phonon populations remain close to local thermal equilibrium and the specific nonequilibrium scenario associated with optical heating does not arise. Similarly, techniques such as time-domain thermoreflectance (TDTR) can provide reliable TBR measurements, as the channel material in this case is also indirectly heated by a transducer layer, where all of the phonons tend to quickly achieve local thermal equilibrium.

In this work, we investigate heat dissipation in ITO devices on sapphire substrates. A monolayer of MoS_2 serves as an in situ sensor to monitor the device temperature during operation using Raman thermometry since the amorphous ITO layer itself does not have any distinct Raman peaks. To quantify interfacial thermal transport, we employ a differential TDTR technique, which can provide better accuracy in the TBR measurements in heterogeneous stacks. Our work provides the first experimental determination of the TBR of an oxide semiconductor−transition metal dichalcogenide interface, revealing very high-quality interfaces in our device stack with TBR in the lower range of other previously reported 2D material interfaces. Furthermore, the independently measured TBR and device electrical characteristics are incorporated in steady state finite-element simulations to compute the MoS_2 temperature during device operation, which agree well with our thermometry experiments, thereby validating our thermal model. Once validated, this model is then used to determine the ITO channel temperature, which cannot be directly accessed by Raman. By obtaining the device temperature and interface properties from independent measurements, our methodology decouples the thermometry from the interface property measurement and provides a more robust framework to analyze heat dissipation across 2D material interfaces and devices. Using this framework, in turn, highlights the centrality of interfacial thermal resistances and heat spreading through the substrate on the heat dissipation of scaled oxide transistors.

Figure 1a illustrates the ITO device structure along with the experimental setup for micro-Raman thermometry during

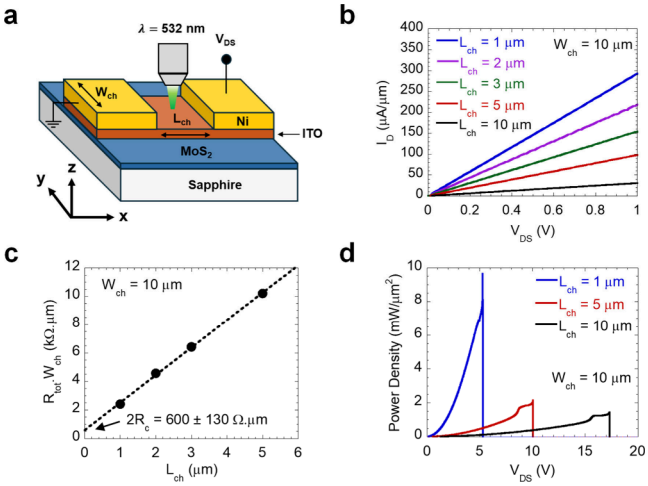

Figure 1. Electrical characteristics and high-field breakdown of ITO devices. (a) Schematic of the ITO device structure with an interfacial monolayer of MoS_2 and the experimental setup for Raman thermometry. (b) I_D−V_{DS} characteristics of 10 μm wide devices with varying channel lengths. The channel consists of 10 nm thick ITO on monolayer MoS_2. (c) TLM plot showing total resistance as a function of channel length. The intercept of linear fit yields the electrical contact resistance. (d) Breakdown behavior of ITO devices with varying channel lengths at high V_{DS}. All measurements are performed at room temperature without gate bias.

device operation. A ∼10 nm-thick ITO layer is sputtered onto monolayer MoS_2 grown on sapphire substrates, followed by deposition of Ni contacts and ITO channel isolation. Over 50 devices are fabricated and characterized with varying channel lengths (L_{ch}) and widths (W_{ch}) ranging from 1 to 20 μm. More details of device fabrication are provided in the Methods section. The I_D−V_{DS} characteristics of 10 μm wide ITO devices with varying channel lengths from 1 to 10 μm, normalized by the channel width, are presented in Figure 1b. The electrical contact resistance R_c of the devices is extracted at room temperature using the transfer length method (TLM). Figure 1c shows the total resistance normalized by width (i.e., $R_{tot}\cdot W_{ch}$) as a function of L_{ch}, where the intercept of the linear fit yields a low total electrical contact resistance, $2R_c = 600 \pm 130$ $\Omega\cdot\mu$m.

A subset of the devices was powered to increasing levels until a breakdown occurred. Resulting power versus drive voltage curves are provided in Figure 1d, where a sharp escalation in power density (PD) is observed at higher V_{DS} followed by an abrupt drop and complete device failure. Atomic force microscopy (AFM) scans of multiple devices after breakdown are presented in Supplementary Note 1, revealing physical damage concentrated near the center of the channel. This observation suggests uniform heating and electric-field distribution within the channel during operation, consistent with the low contact resistance of the devices.[40]

To probe the temperature of the ITO devices under operation, the applied drain-bias to the device is gradually increased every few minutes while simultaneously collecting Raman spectra at each voltage at the center of the device channel. The temperature-dependence of the Raman peak shifts of MoS_2 is used to determine the device temperature. The detailed measurement procedure is described later in the text and in Supplementary Note 2. The time history of a representative device with channel length and width of 1 μm is

https://doi.org/10.1021/acs.nanolett.5c05421
Nano Lett. XXXX, XXX, XXX−XXX

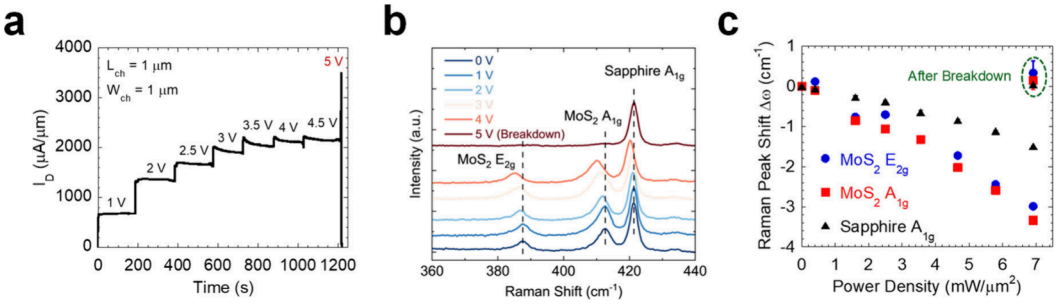

Figure 2. Drain bias-dependent Raman spectra of ITO devices under operation. (a) The current history of an ITO device with channel length and width of 1 μm, indicating significant self-heating effect at high V_{DS}. (b) The corresponding Raman spectra at the center of the device channel as a function of V_{DS}. (c) The extracted Raman peak shifts ($\Delta\omega$) of the MoS_2 E_{2g}, MoS_2 A_{1g}, and Sapphire A_{1g} peaks. The redshift of the Raman peaks with increasing V_{DS} indicates device heating until the onset of breakdown at V_{DS} = 5 V, where the Raman peaks return close to the original measurement at V_{DS} = 0 V (encircled in green).

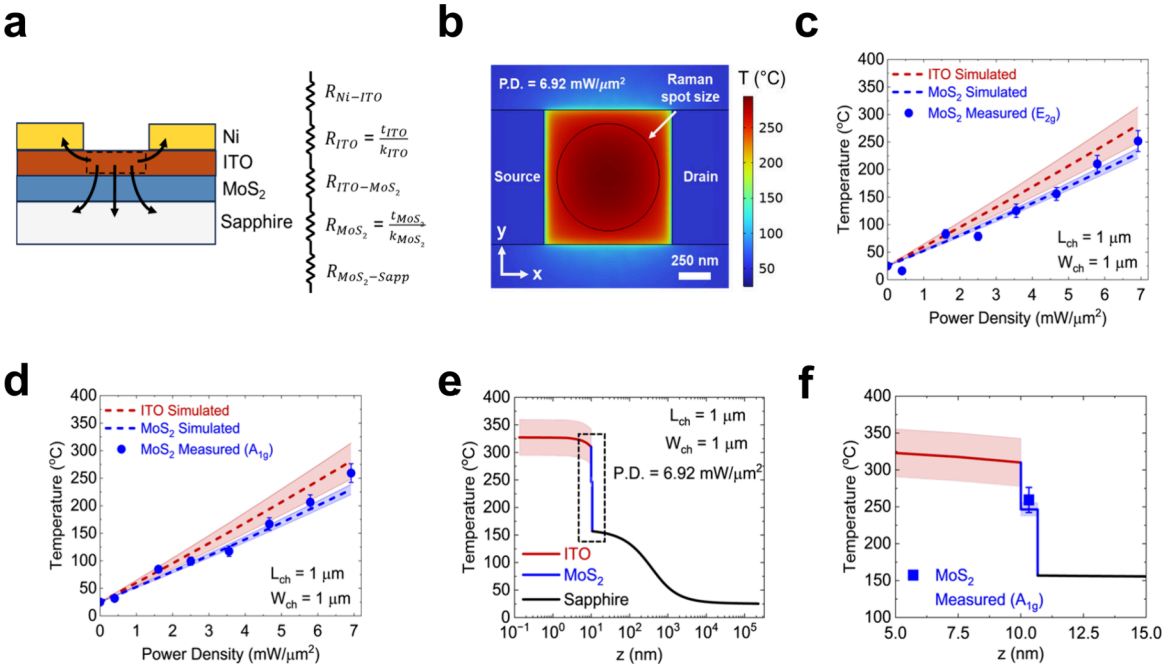

Figure 3. Finite-element simulations of the ITO devices and comparison against Raman thermometry measurements. (a) Schematic of the ITO device structure and heat dissipation pathways during operation along with a simplified thermal resistor network for vertical heat flow during the TDTR measurements. (b) Temperature map of the 1 μm × 1 μm device presented in Figure 2 simulated in COMSOL at an input PD of 6.92 mW/μm^2. The simulated temperature of the ITO and MoS_2 layers at the center of the device channel as a function of input PD was compared against the measured MoS_2 temperature using the (c) E_{2g} and (d) A_{1g} Raman peaks, respectively. (e) Simulated vertical temperature profile of the device at the center of the channel. The dashed region of interest is zoomed-in and shown in (f), which also presents the MoS_2 temperature measured using the A_{1g} Raman mode, and the temperature drops across different interfaces due to their thermal boundary resistances (TBR). The shaded regions represent the uncertainty in the simulated temperature profile due to the uncertainty in TBR measurement. The measured and simulated temperature at the center of the channel is a Gaussian-weighted average over the Raman spot size, as illustrated in (b).

presented in Figure 2a, and the corresponding Raman spectra collected are presented in Figure 2b. The extracted Raman shifts of the E_{2g} and A_{1g} mode of MoS_2 along with the A_{1g} mode of sapphire as a function of input PD in the ITO channel are presented in Figure 2c. The PD is calculated after removing the contribution of the device contacts using

$$PD = \frac{I_D(V_{DS} - 2I_D R_c)}{L_{ch} \times W_{ch}} \quad (1)$$

For low bias voltages, the measured current increases approximately linearly with voltage before beginning to saturate around $V_{DS} \sim 3$ V. With a further voltage increase, the current gradually decreases with time, indicating increased scattering and reduced mobility in the ITO device due to the presence of significant self-heating. Concurrently, a substantial redshift of the MoS_2 and sapphire Raman peaks is observed, as shown in Figure 2b, suggesting a significant temperature rise in the ITO channel and large heat flow across the MoS_2 layer and into the sapphire substrate. Upon further increasing the V_{DS} to ~5 V, the current exhibits a sharp increase followed by an abrupt drop, culminating in complete device breakdown. Notably, the Raman peaks of both MoS_2 and sapphire immediately return close to their initial positions at zero bias after breakdown, as highlighted in Figure 2c. This recovery confirms that the heat source (i.e., the ITO channel) has been turned off and the device stack has cooled down to room temperature. Additionally, a significant reduction in the

https://doi.org/10.1021/acs.nanolett.5c05421
Nano Lett. XXXX, XXX, XXX−XXX

intensity of the MoS_2 peaks is evident, suggesting either damage in the MoS_2 itself or the ITO, which acts to reduce the collection efficiency of the Raman scattered light. Both observations are consistent with the topographical changes observed with AFM. On the other hand, the intensity of the MoS_2 peaks remains prominent near the contacts, where AFM scans reveal no significant damage, as shown in Supplementary Note 1.

To analyze the heat dissipation in the ITO devices, we perform three-dimensional finite-element simulations in COMSOL, with the modeling details provided in Supplementary Notes 3 and 4. The simulation assumes uniform volumetric heat generation across the ITO channel, which is a good approximation near the linear regime. A schematic of the ITO device structure is provided in Figure 3a along with the heat dissipation pathways during operation, which are primarily limited by the TBR of different interfaces and heat spreading into the sapphire substrate. In previous studies, the TBR was usually estimated (rather than directly measured) from the channel temperature, inherently coupling both parameters together and limiting the independent validation of the temperature measurements. Here, we employed a differential TDTR technique to directly measure the TBR of all interfaces within our device stack, with the results presented in Table 1. A detailed description of the differential TDTR measurements is provided in the Methods section, and a comprehensive uncertainty analysis is provided in Supplementary Note 3. A simplified thermal resistor network for vertical heat flow through the complete device stack during the TDTR measurements is presented in Figure 3a. The measurements indicate very high-quality interfaces in our device stack, with TBR values at the lower end of the range reported for other 2D material interfaces.[9,35,36,39,41] The measured TBR is then input into our 3D finite-element model to compute the thermal behavior of the device and compared with the experimentally measured device temperatures acquired using Raman spectroscopy. The simulated temperature map of the device shown in Figure 2c at an input PD of 6.92 mW/μm^2 (corresponding to $V_{DS} \sim 4.5$ V) is presented in Figure 3b.

Table 1. Thermal Boundary Resistance of Interfaces in the ITO/MoS_2/Sapphire Device Stack

Interface	Thermal Boundary Resistance ($\times 10^{-8}$ m^2 K/W)
Ni-ITO	0.38 ± 0.03
ITO-MoS_2	0.58 ± 0.34
MoS_2-Sapphire	1.17 ± 0.13

The temperature rise in the monolayer MoS_2 during device operation can be deduced by utilizing the temperature-dependence of its Raman peak shifts ($\Delta\omega$) as a noncontact optical thermometer. However, it is important to note that measured shifts in Figure 2c arise not only from intrinsic temperature effects but also from the strain induced by the thermal expansion mismatch between MoS_2 and the surrounding materials during heating. To accurately quantify the MoS_2 temperature, it is, therefore, essential to decouple and remove this strain-dependent Raman contribution. In our previous work,[22] we demonstrated that the Raman peak position responds linearly to both temperature and strain and can be directly superimposed using the expression

$$\Delta\omega = (\chi_T^o + 2\chi_\epsilon \alpha)\Delta T \quad (2)$$

where χ_T^o is the pure temperature contribution or the "stress-free" temperature coefficient, χ_ϵ is the strain coefficient, and α is the coefficient of thermal expansion (CTE). Crucially, the pure temperature coefficient obtained from this methodology is independent of the particular strain distribution and is applicable as long as the film remains stress-free. To experimentally ensure this stress-free scenario, we transferred monolayer MoS_2 from the sapphire substrate onto a holey SiN membrane, thereby suspending the film. The detailed MoS_2 transfer procedure is provided in the Methods section. The suspended sample releases any thermally generated stress due to buckling,[22,42] ensuring that the MoS_2 film remains stress-free during heating. Calibration of the pure temperature-induced Raman shifts was then performed using this suspended MoS_2 sample, with the corresponding results provided in Supplementary Note 2.

The temperature of the MoS_2 layer in the device shown in Figure 2c is determined from the Raman peak shifts by using the stress-free temperature coefficient. Temperatures calculated using the E_{2g} and A_{1g} Raman modes of MoS_2 at the center of the device channel are presented as a function of input PD in Figure 3c and 3d, respectively, along with the corresponding temperature of the ITO and MoS_2 layers predicted by the COMSOL simulations. Both measured and simulated temperatures at the center of the channel are Gaussian-weighted and averaged over the Raman spot size. Previous studies have established that the positions of the E_{2g} and A_{1g} Raman modes are highly sensitive to the strain and doping levels in monolayer MoS_2.[26,43,44] As shown in Figure 3c and 3d, the MoS_2 temperatures calculated from both Raman modes agree closely with each other and with the simulation results, indicating that our temperature calibration methodology can effectively eliminate strain and doping-related Raman shift contributions from the thermometry. Furthermore, the simulation, which utilizes the measured electrical characteristics of the device and TBR of all interfaces as input parameters, independently validates our thermometry.

The simulated vertical temperature profile across the device stack at the center of the ITO channel under an input PD of 6.92 mW/μm^2 is presented in Figure 3e and 3f. The shaded regions reflect the uncertainty in the predicted temperature profile derived by propagating the uncertainty in the measured TBR into the simulations. We also present the measured MoS_2 temperature using the A_{1g} Raman mode in Figure 3f, as the A_{1g} mode is considered more reliable for thermometry.[19,45,46] The vertical temperature profile reveals that the heat dissipation into the substrate is strongly influenced by heat transport across interfaces (rather than through the thin channel materials) and emphasizes the importance of direct and accurate TBR measurements. Moreover, since in our devices L_{ch} is much larger than the thermal healing length, the characteristic lateral distance over which temperature decays from the contacts (which is typically on the order of hundreds of nm),[41,47,48] the overall thermal resistance of the structure is dominated by the heat spreading into the sapphire substrate ($R_{Sapphire} \approx \sqrt{L_{ch}W_{ch}}/2k_{Sapphire}$).[19,49]

Thermometry line scans were conducted across the ITO channel during device operation to assess the effect of the lateral heat dissipation into the device contacts. Results for a device with channel length and width of 2 μm are presented in Figure 4. Figure 4a presents the measured MoS_2 temperature

https://doi.org/10.1021/acs.nanolett.5c05421
Nano Lett. XXXX, XXX, XXX−XXX

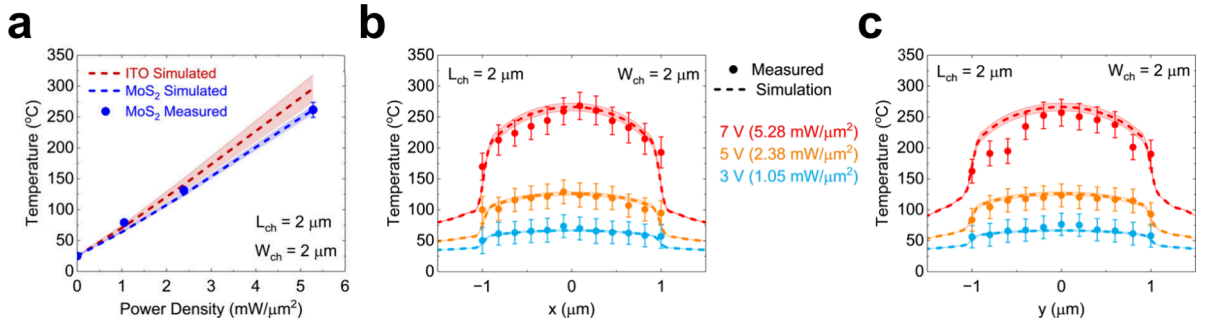

Figure 4. Measured temperature profile of ITO devices. (a) The simulated temperature of the ITO and MoS_2 layers at the center of a 2 μm × 2 μm device channel compared against the measured MoS_2 A_{1g} temperature at varying input PD. The evolution of the MoS_2 temperature profile along the device channel (b) length and (c) width with increasing PD. The shaded regions represent the uncertainty in the simulated temperature profile due to the uncertainty in TBR measurement.

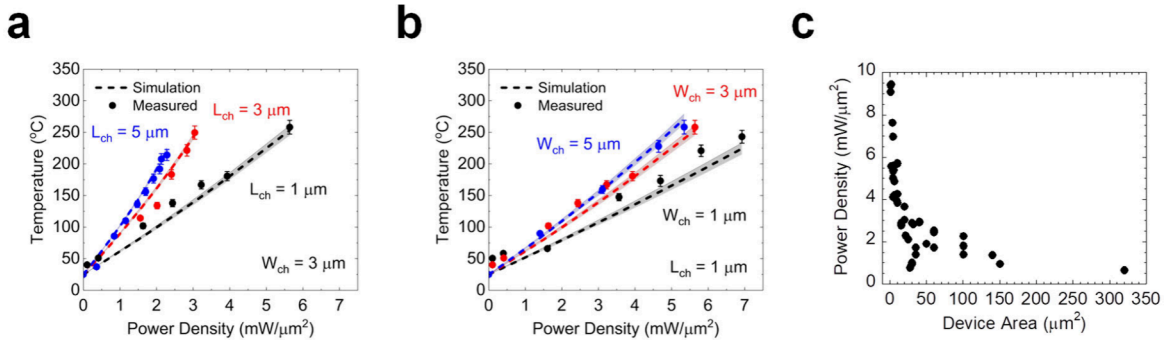

Figure 5. Channel length- and width-dependent heat dissipation in ITO devices. The measured and simulated temperature at the center of the device inside the MoS_2 layer with (a) a channel width of 3 μm and varying length of 1, 3, and 5 μm and (b) channel length of 1 μm and varying width of 1, 3, and 5 μm. All devices were measured until the onset of device breakdown. (c) The measured breakdown PD of multiple devices as a function of the device area.

at the channel center and comparison against the simulation at varying input PD. Correspondingly, Raman thermometry line scans were performed along the channel length and width, and the resulting spatial temperature profiles are presented in Figure 4b and c, respectively. At the highest input PD of 5.28 mW/μm^2, the measured data reflect the device behavior just before breakdown. Here, a slight deviation between the measured and simulated temperature is observed, suggesting nonuniform heating in the channel preceding breakdown. After breakdown, AFM scans reveal cracks in the device tend to nucleate near the center of the channel and across the channel width, as presented in Supplementary Note 1. Such structural degradation likely creates intrinsic variability that is more pronounced in the transverse direction than in the longitudinal direction, resulting in the more irregular temperature profiles observed in Figure 4c. Additionally, the possibility of any initial surface defects on the ITO channel and gradual crack formation in the devices at lower input PD is also considered, which may get exacerbated during complete breakdown, with the results presented in Supplementary Note 5.

The influence of channel length and width on the heat dissipation in ITO devices up to breakdown is also systematically investigated. Figure 5a presents the measured MoS_2 temperature at the channel center for devices with a fixed width of 3 μm and varying length of 1, 3, and 5 μm. The measured MoS_2 temperatures at the channel center for devices with a fixed length of 1 μm and varying width of 1, 3, and 5 μm are presented in Figure 5b. The results show that reducing the channel area allows the devices to sustain higher PD before breakdown, and for a given PD, smaller devices exhibit a lower temperature rise at the channel center.

Since all the channel dimensions studied here are much larger than the thermal healing length, the primary origin of this cooling effect with reduced device size is the decrease in the effective vertical spreading resistance into the sapphire substrate ($R_{Sapphire} \approx \sqrt{L_{ch}W_{ch}}/2k_{Sapphire}$). In this geometry, any lateral heat removal through the Ni contacts or channel edges plays only a minor role. The measured breakdown PD of more than 40 devices as a function of device area is presented in Figure 5c. These findings confirm that the device geometry plays a pivotal role in the thermal management and reliability of our ITO devices. Furthermore, at device breakdown, the average temperature of the MoS_2 and ITO layers is found to be below the critical threshold typically required to instigate thermal damage in these materials, implying the possibility of other mechanisms contributing to device breakdown, which are discussed in Supplementary Note 5.

In conclusion, this work presents a comprehensive investigation of heat dissipation in ITO devices on sapphire substrates, employing a MoS_2 monolayer as an in situ Raman sensor to monitor device temperature during operation. The TBRs of all interfaces in the device stack are directly measured using TDTR, rather than estimated from thermometry. Our findings reveal high-quality interfaces with TBR values among the lowest reported for 2D material systems, enabling the ITO devices to sustain large power densities (PD > 9 mW/μm^2) before breakdown. Finite-element simulations incorporating the measured electrical device characteristics and TBR

https://doi.org/10.1021/acs.nanolett.5c05421
Nano Lett. XXXX, XXX, XXX−XXX

independently validate Raman thermometry. Our approach decouples the thermometry from interface characterization, offering a robust framework for analyzing heat dissipation in heterogeneous device stacks. Systematic device measurements and simulations further show that channel geometry significantly impacts thermal management and breakdown behaviors, with smaller devices exhibiting enhanced heat dissipation and higher breakdown thresholds. The spatial temperature profiles and breakdown locations identified in this study emphasize the critical role of interface thermal properties and substrate heat spreading on the device reliability. Ultimately, our integrated thermometry and thermal interface quantification approach paves the way for more robust and accurate thermal assessments and improved design of thin-film nanoelectronics, including not only those of ITO but also those of Si and 2D-materials as well.

METHODS

Device Fabrication

Monolayer MoS_2 grown on sapphire substrates was provided by IMEC Belgium. Ten nm thick indium tin oxide (ITO) was deposited using RF sputtering with a composition of 90 wt % In_2O_3 and 10 wt % SnO_2. The sputtering power was 650 W in ambient argon with a working pressure of 2 mTorr. 100 nm Ni was deposited by e-beam evaporation as source/drain contacts, patterned by electron beam lithography with channel lengths (L_{ch}) and widths (W_{ch}) ranging from 1 to 20 μm. Finally, channel isolation was performed by plasma dry etching of ITO with BCl_3 and Ar. For the TDTR measurements, 100 nm Ni was deposited as the transducer layer by e-beam evaporation. All material stacks were processed in the same batch to ensure a similar quality of metal deposition. As-grown monolayer MoS_2 was wet transferred from sapphire onto the holey SiN membrane by using a polystyrene solution.

Electrical Characterization

Electrical measurements were performed using a Keithley 4200A parameter analyzer with a Cascade MPS150 probe station, in air and room temperature ambient. AFM scans were performed by using a home-built AFM system (AIST-NT).

Micro-Raman Thermometry

A HORIBA LabRAM HR800 Raman spectrometer equipped with a 532 nm wavelength laser was used for all Raman and photoluminescence measurements. The laser was focused on the samples using a long working distance 50× objective (N.A. = 0.55) to a spot size of ~0.8 μm. The temperature calibrations of the samples were performed inside a Linkam THMS720 heating stage during both heating and cooling cycles, and the absorbed laser power was kept low to minimize laser-induced heating effects. The acquired Raman spectra were fitted using a Lorentzian function to extract the Raman peak positions. The grating used has a groove density of 1800 l/mm, which gives a nominal spectral resolution of 0.27 cm^{-1} per pixel. The Lorentzian peak fitting yields a peak position shift uncertainty of less than 0.02 cm^{-1} for the MoS_2 A_{1g} peak, corresponding to a temperature increase measurement uncertainty of around 1 K.

During Raman thermometry, the bias voltage was applied by using a Keithley 2612A DC source meter. Using micromanipulators, tungsten probe tips were carefully brought into physical contact with the source and drain pads of the device under test. A low-noise source-measure unit (SMU) from Keithley supplied the DC source−drain bias and recorded the corresponding drain current. A low-voltage test is first performed to check for probing and device fabrication issues. During each thermometry experiment, the current history of the device was continuously recorded by using a LabVIEW-based data acquisition program. Before starting the optical measurements at a given bias, we allowed several seconds for the electrical current and device temperature to reach a steady state. More details of the Raman thermometry are provided in Supplementary Note 2.

Time-Domain Thermoreflectance Measurements

Thermal boundary resistances (TBR) of the interfaces in our device stack were measured using a home-built femtosecond time-domain thermoreflectance (TDTR) setup. A Coherent Mira 900 fs laser is used to generate a 200 fs, 78 MHz beam at 800 nm wavelength. The output beam is split into a pump beam and a probe beam. The pump is directed into an electro-optical modulator (EOM) driven at a frequency of 1.3 MHz and then frequency-doubled by focusing onto a bismuth borate (BBO) crystal to produce 400 nm light. The probe beam is modulated by a 280 Hz mechanical chopper and passed through a 4-pass delay line. The size of the pump and probe beam focused on the sample was characterized by knife-edge measurements. The reflected probe beam from the sample is collected by a photodetector and high-frequency lock-in amplifier, followed by a digital lock-in mechanism. A heat transfer model was used to fit the ratio curve obtained from the TDTR measurement. The measurements were repeated several times at different locations across the samples to ensure repeatability.

A differential TDTR technique was utilized to measure the TBR of all interfaces within our device stack. In this differential approach, a series of device structures were prepared, each terminated at successive fabrication steps, thereby isolating specific "buried" interfaces for targeted measurements (e.g., the MoS_2/Sapphire interface). This differential strategy enables much greater precision in quantifying the individual resistances in the complicated device stack, albeit with the presumption that the interfacial properties are nominally equivalent among the differing physical samples. Close correlation between the measured values and modeling when using these parameters supports the veracity of this presumption. More details of the TDTR measurements along with an uncertainty analysis are provided in Supplementary Note 3.

ASSOCIATED CONTENT

Supporting Information

The Supporting Information is available free of charge at https://pubs.acs.org/doi/10.1021/acs.nanolett.5c05421.

1. AFM scans after device breakdown, 2. temperature-dependent Raman spectroscopy of suspended monolayer MoS_2, 3. thermal interface resistance determined by TDTR and uncertainty analysis, 4. finite-element simulations and temperature rise due to laser heating, 5. sequential AFM scans after device operation (PDF)

AUTHOR INFORMATION

Corresponding Authors

Peide D. Ye − *Birck Nanotechnology Center and Elmore Family School of Electrical and Computer Engineering, Purdue University, West Lafayette, Indiana 47907, United States;* orcid.org/0000-0001-8466-9745; Email: yep@purdue.edu

Xianfan Xu − *School of Mechanical Engineering, Birck Nanotechnology Center, and Elmore Family School of Electrical and Computer Engineering, Purdue University, West Lafayette, Indiana 47907, United States;* orcid.org/0000-0003-0580-4625; Email: xxu@ecn.purdue.edu

Authors

Neil Ghosh − *School of Mechanical Engineering and Birck Nanotechnology Center, Purdue University, West Lafayette, Indiana 47907, United States;* orcid.org/0000-0002-0527-011X

Zehao Lin − *Birck Nanotechnology Center and Elmore Family School of Electrical and Computer Engineering, Purdue University, West Lafayette, Indiana 47907, United States*

https://doi.org/10.1021/acs.nanolett.5c05421
Nano Lett. XXXX, XXX, XXX−XXX

Monoranjan Debnath Rony − *School of Mechanical Engineering and Birck Nanotechnology Center, Purdue University, West Lafayette, Indiana 47907, United States*
Sahej Sharma − *School of Mechanical Engineering and Birck Nanotechnology Center, Purdue University, West Lafayette, Indiana 47907, United States*
Jian-Yu Lin − *Birck Nanotechnology Center and Elmore Family School of Electrical and Computer Engineering, Purdue University, West Lafayette, Indiana 47907, United States;* orcid.org/0000-0002-8800-8714
Zheng Sun − *Birck Nanotechnology Center and Elmore Family School of Electrical and Computer Engineering, Purdue University, West Lafayette, Indiana 47907, United States;* orcid.org/0000-0002-8620-1262
Zhihong Chen − *Birck Nanotechnology Center and Elmore Family School of Electrical and Computer Engineering, Purdue University, West Lafayette, Indiana 47907, United States*
Joerg Appenzeller − *Birck Nanotechnology Center and Elmore Family School of Electrical and Computer Engineering, Purdue University, West Lafayette, Indiana 47907, United States*
Thomas E. Beechem − *School of Mechanical Engineering and Birck Nanotechnology Center, Purdue University, West Lafayette, Indiana 47907, United States;* orcid.org/0000-0002-7536-0719

Complete contact information is available at: https://pubs.acs.org/10.1021/acs.nanolett.5c05421

Author Contributions

N.G., Z.L., and M.D.R. contributed equally to this work. P.D.Y. and X.X. conceived the idea and supervised the project. Z.L. and J.Y.L. fabricated the devices. N.G. and Z.L. performed the electrical measurements. N.G. performed the Raman thermometry and the COMSOL simulations, supported by S.S. and T.E.B. M.D.R. performed the TDTR measurements. Z.S. prepared the suspended MoS_2 samples under the supervision of Z.C., and J.A. N.G., and M.D.R. analyzed the experimental data. N.G. and X.X. cowrote the manuscript with input from all authors.

Notes

The authors declare no competing financial interest.

■ ACKNOWLEDGMENTS

The authors would like to thank Daniel C. Hayes and Rakesh Agrawal for support with the ITO sputtering. N.G. acknowledges valuable discussions and technical support from Chang Niu and Junwoo Jang. This work was funded by the Semiconductor Research Cooperation (SRC) Global Research Collaboration (GRC) Program and through the joint MOU between the Indiana Economic Development Corporation, Purdue University, and imec with in-kind support from the Applied Research Institute.

■ REFERENCES

(1) Nomura, K.; Ohta, H.; Takagi, A.; Kamiya, T.; Hirano, M.; Hosono, H. Room-Temperature Fabrication of Transparent Flexible Thin-Film Transistors Using Amorphous Oxide Semiconductors. *Nature* **2004**, *432* (7016), 488−492.
(2) Nomura, K.; Takagi, A.; Kamiya, T.; Ohta, H.; Hirano, M.; Hosono, H. Amorphous Oxide Semiconductors for High-Performance Flexible Thin-Film Transistors. *Jpn. J. Appl. Phys.* **2006**, *45* (5S), 4303.
(3) Si, M.; Lin, Z.; Chen, Z.; Sun, X.; Wang, H.; Ye, P. D. Scaled Indium Oxide Transistors Fabricated Using Atomic Layer Deposition. *Nat. Electron.* **2022**, *5* (3), 164−170.
(4) Si, M.; Hu, Y.; Lin, Z.; Sun, X.; Charnas, A.; Zheng, D.; Lyu, X.; Wang, H.; Cho, K.; Ye, P. D. Why In2O3 Can Make 0.7 Nm Atomic Layer Thin Transistors. *Nano Lett.* **2021**, *21* (1), 500−506.
(5) Li, S.; Tian, M.; Gao, Q.; Wang, M.; Li, T.; Hu, Q.; Li, X.; Wu, Y. Nanometre-Thin Indium Tin Oxide for Advanced High-Performance Electronics. *Nat. Mater.* **2019**, *18* (10), 1091−1097.
(6) Zhang, Z.; Hu, Y.; Lin, Z.; Si, M.; Charnas, A.; Cho, K.; Ye, P. D. Atomically Thin Indium-Tin-Oxide Transistors Enabled by Atomic Layer Deposition. *IEEE Trans. Electron Devices* **2022**, *69* (1), 231−236.
(7) Si, M.; Andler, J.; Lyu, X.; Niu, C.; Datta, S.; Agrawal, R.; Ye, P. D. Indium-Tin-Oxide Transistors with One Nanometer Thick Channel and Ferroelectric Gating. *ACS Nano* **2020**, *14* (9), 11542−11547.
(8) Si, M.; Murray, A.; Lin, Z.; Andler, J.; Li, J.; Noh, J.; Alajlouni, S.; Niu, C.; Lyu, X.; Zheng, D.; Maize, K.; Shakouri, A.; Datta, S.; Agrawal, R.; Ye, P. D. BEOL Compatible Indium-Tin-Oxide Transistors: Switching of Ultrahigh-Density 2-D Electron Gas over 0.8 × 1014/Cm2at Oxide/Oxide Interface by the Change of Ferroelectric Polarization. *IEEE Trans. Electron Devices* **2021**, *68* (7), 3195−3199.
(9) Su, H.; Lee, Y. M.; Peña, T.; Fultz-Waters, S.; Kang, J.; Köroğlu, Ç.; Wahid, S.; Newcomb, C. J.; Song, Y. S.; Wong, H. S. P.; Wang, S. X.; Pop, E. High-Field Breakdown and Thermal Characterization of Indium Tin Oxide Transistors. *ACS Nano* **2025**, *19* (17), 16794−16802.
(10) Deng, S.; Kwak, J.; Lee, J.; Aabrar, K. A.; Kim, T.-H.; Choe, G.; Kirtania, S. G.; Zhang, C.; Li, W.; Phadke, O.; Yu, S.; Datta, S. BEOL Compatible Oxide Power Transistors for On- Chip Voltage Conversion in Heterogenous 3D (H3D) Integrated Circuits. *In 2023 International Electron Devices Meeting (IEDM)*; IEEE, 2023; pp 1−4 DOI: 10.1109/IEDM45741.2023.10413838.
(11) Kwak, J.; Shin, J.; Deng, S.; Jeong, G.; Sharda, J.; Datta, S.; Yu, S. Bias Temperature Instability Analysis of Oxide Power Transistors for BEOL On-Chip Voltage Converter in Thermally-Constrained H3D Systems. In *2024 IEEE International Electron Devices Meeting (IEDM)*; IEEE, 2024; pp 1−4 DOI: 10.1109/IEDM50854.2024.10873303.
(12) Hu, Q.; Zhu, S.; Zhu, Y.; Gu, C.; Liu, S.; Huang, R.; Wu, Y. Amorphous Indium Tin Oxide Transistors for Power Amplification above 10 GHz. *Nat. Electron.* **2025**, *8* (9), 803−809.
(13) Zhou, H.; Zhang, K.; Hong, P.; Zhou, M.; Gao, G.; Xiang, M.; Liu, Z.; Li, X.; Si, M.; Hao, Y.; Zhang, J. First Demonstration of Top T-Gate Beol-Compatible Indium-Oxide RF Transistors with Record Maximum Oscillation Frequency of 70 GHz. In *2025 Symposium on VLSI Technology and Circuits (VLSI Technology and Circuits)*; IEEE, 2025; pp 1−3 DOI: 10.23919/VLSITechnologyandCir65189.2025.11074889.
(14) Liao, P. Y.; Khot, K.; Alajlouni, S.; Snure, M.; Noh, J.; Si, M.; Zhang, Z.; Shakouri, A.; Ruan, X.; Ye, P. D. Alleviation of Self-Heating Effect in Top-Gated Ultrathin In2O3 FETs Using a Thermal Adhesion Layer. *IEEE Trans. Electron Devices* **2023**, *70* (1), 113−120.
(15) Lin, J.-Y.; Zhang, Z.; Alajlouni, S.; Liao, P.-Y.; Lin, Z.; Niu, C.; Shakouri, A.; Ye, P. D. First Determination of Thermal Resistance and Thermal Capacitance of Atomic-Layer-Deposited In_2O_3 Transistors. In *2023 International Electron Devices Meeting (IEDM)*; IEEE, 2023; pp 1−4 DOI: 10.1109/IEDM45741.2023.10413835.
(16) Liao, P.-Y.; Alajlouni, S.; Si, M.; Zhang, Z.; Lin, Z.; Noh, J.; Wilk, C.; Shakouri, A.; Ye, P. D. Thermal Studies of BEOL-Compatible Top-Gated Atomically Thin ALD In2O3 FETs. In *2022 IEEE Symposium on VLSI Technology and Circuits (VLSI Technology and Circuits)*; IEEE, 2022; pp 322−323 DOI: 10.1109/VLSITechnologyandCir46769.2022.9830279.

(17) Liao, P.-Y.; Zheng, D.; Alajlouni, S.; Zhang, Z.; Si, M.; Zhang, J.; Lin, J.-Y.; Feygelson, T. I.; Tadjer, M. J.; Shakouri, A.; Ye, P. D. Transient Thermal and Electrical Co-Optimization of BEOL Top-Gated ALD In2O3 FETs Toward Monolithic 3-D Integration. *IEEE Trans. Electron Devices* **2023**, *70* (4), 2052−2058.
(18) Kise, K.; Fujii, M. N.; Bermundo, J. P.; Ishikawa, Y.; Uraoka, Y. Self-Heating Suppressed Structure of a-IGZO Thin-Film Transistor. *IEEE Electron Device Lett.* **2018**, *39* (9), 1322−1325.
(19) Yalon, E.; McClellan, C. J.; Smithe, K. K. H.; Muñoz Rojo, M.; Xu, R. L.; Suryavanshi, S. V.; Gabourie, A. J.; Neumann, C. M.; Xiong, F.; Farimani, A. B.; Pop, E. Energy Dissipation in Monolayer MoS2 Electronics. *Nano Lett.* **2017**, *17* (6), 3429−3433.
(20) Beechem, T.; Graham, S.; Kearney, S. P.; Phinney, L. M.; Serrano, J. R. Invited Article: Simultaneous Mapping of Temperature and Stress in Microdevices Using Micro-Raman Spectroscopy. *Rev. Sci. Instrum.* **2007**, *78* (6), DOI: 10.1063/1.2738946.
(21) Beechem, T.; Christensen, A.; Graham, S.; Green, D. Micro-Raman Thermometry in the Presence of Complex Stresses in GaN Devices. *J. Appl. Phys.* **2008**, *103* (12), DOI: 10.1063/1.2940131.
(22) Huang, S.; Chen, Y.; Luo, Z.; Xu, X. Temperature and Strain Effects in Micro-Raman Thermometry for Measuring In-Plane Thermal Conductivity of Thin Films. *Nanoscale and Microscale Thermophysical Engineering* **2021**, *25* (2), 91−100.
(23) Beechem, T.; Christensen, A.; Green, D. S.; Graham, S. Assessment of Stress Contributions in GaN High Electron Mobility Transistors of Differing Substrates Using Raman Spectroscopy. *J. Appl. Phys.* **2009**, *106* (11), DOI: 10.1063/1.3267157.
(24) Michail, A.; Delikoukos, N.; Parthenios, J.; Galiotis, C.; Papagelis, K. Optical Detection of Strain and Doping Inhomogeneities in Single Layer MoS2. *Appl. Phys. Lett.* **2016**, *108* (17), DOI: 10.1063/1.4948357.
(25) Bruna, M.; Ott, A. K.; Ijäs, M.; Yoon, D.; Sassi, U.; Ferrari, A. C. Doping Dependence of the Raman Spectrum of Defected Graphene. *ACS Nano* **2014**, *8* (7), 7432−7441.
(26) Velický, M.; Rodriguez, A.; Bouša, M.; Krayev, A. V.; Vondráček, M.; Honolka, J.; Ahmadi, M.; Donnelly, G. E.; Huang, F.; Abruña, H. D.; Novoselov, K. S.; Frank, O. Strain and Charge Doping Fingerprints of the Strong Interaction between Monolayer MoS2 and Gold. *J. Phys. Chem. Lett.* **2020**, *11* (15), 6112−6118.
(27) Schmidt, D. A.; Ohta, T.; Beechem, T. E. Strain and Charge Carrier Coupling in Epitaxial Graphene. *Phys. Rev. B* **2011**, *84* (23), No. 235422.
(28) Luo, Z.; Liu, H.; Spann, B. T.; Feng, Y.; Ye, P.; Chen, Y. P.; Xu, X. Measurement of In-Plane Thermal Conductivity of Ultrathin Films Using Micro-Raman Spectroscopy. *Nanoscale and Microscale Thermophysical Engineering* **2014**, *18* (2), 183−193.
(29) Yan, R.; Simpson, J. R.; Bertolazzi, S.; Brivio, J.; Watson, M.; Wu, X.; Kis, A.; Luo, T.; Hight Walker, A. R.; Xing, H. G. Thermal Conductivity of Monolayer Molybdenum Disulfide Obtained from Temperature-Dependent Raman Spectroscopy. *ACS Nano* **2014**, *8* (1), 986−993.
(30) Luo, Z.; Maassen, J.; Deng, Y.; Du, Y.; Garrelts, R. P.; Lundstrom, M. S.; Ye, P. D.; Xu, X. Anisotropic In-Plane Thermal Conductivity Observed in Few-Layer Black Phosphorus. *Nat. Commun.* **2015**, *6* (1), 8572.
(31) Huang, S.; Ghosh, N.; Niu, C.; Chen, Y. P.; Ye, P. D.; Xu, X. Optically Gated Electrostatic Field-Effect Thermal Transistor. *Nano Lett.* **2024**, *24* (17), 5139−5145.
(32) Beechem, T.; Yates, L.; Graham, S. Invited Review Article: Error and Uncertainty in Raman Thermal Conductivity Measurements. *Rev. Sci. Instrum.* **2015**, *86* (4), DOI: 10.1063/1.4918623.
(33) Ghosh, N.; Chen, Y. P.; Xu, X. Nanostructuring Enables Greatly Suppressed Thermal Conductivity and Enhanced Thermoelectric Performance in Topological Insulator Thin Films. *ACS Appl. Mater. Interfaces* **2025**, *17* (47), 64831−64841.
(34) Freitag, M.; Steiner, M.; Martin, Y.; Perebeinos, V.; Chen, Z.; Tsang, J. C.; Avouris, P. Energy Dissipation in Graphene Field-Effect Transistors. *Nano Lett.* **2009**, *9* (5), 1883−1888.
(35) Yalon, E.; Aslan, Ö. B.; Smithe, K. K. H.; McClellan, C. J.; Suryavanshi, S. V.; Xiong, F.; Sood, A.; Neumann, C. M.; Xu, X.; Goodson, K. E.; Heinz, T. F.; Pop, E. Temperature-Dependent Thermal Boundary Conductance of Monolayer MoS2 by Raman Thermometry. *ACS Appl. Mater. Interfaces* **2017**, *9* (49), 43013−43020.
(36) Xie, J.; Yu, Z.; Sun, Y.; Gan, Q.; Liu, C.; Wang, L.; Zhang, L.; Zhao, Y. Interfacial Thermal Transport and Energy Dissipation in Multilayer PdSe2 Field Effect Transistors. *Adv. Mater.* **2025**, *37* (24), DOI: 10.1002/adma.202503264.
(37) Vaziri, S.; Yalon, E.; Muñoz Rojo, M.; Suryavanshi, S. V.; Zhang, H.; McClellan, C. J.; Bailey, C. S.; Smithe, K. K. H.; Gabourie, A. J.; Chen, V.; Deshmukh, S.; Bendersky, L.; Davydov, A. V.; Pop, E. Ultrahigh Thermal Isolation across Heterogeneously Layered Two-Dimensional Materials. *Sci. Adv.* **2019**, *5* (8), DOI: 10.1126/sciadv.aax1325.
(38) Behranginia, A.; Hemmat, Z.; Majee, A. K.; Foss, C. J.; Yasaei, P.; Aksamija, Z.; Salehi-Khojin, A. Power Dissipation of WSe2 Field-Effect Transistors Probed by Low-Frequency Raman Thermometry. *ACS Appl. Mater. Interfaces* **2018**, *10* (29), 24892−24898.
(39) Zheng, W.; McClellan, C. J.; Pop, E.; Koh, Y. K. Non-equilibrium Phonon Thermal Resistance at MoS2/Oxide and Graphene/Oxide Interfaces. *ACS Appl. Mater. Interfaces* **2022**, *14* (19), 22372−22380.
(40) Mleczko, M. J.; Xu, R. L.; Okabe, K.; Kuo, H. H.; Fisher, I. R.; Wong, H. S. P.; Nishi, Y.; Pop, E. High Current Density and Low Thermal Conductivity of Atomically Thin Semimetallic WTe2. *ACS Nano* **2016**, *10* (8), 7507−7514.
(41) Gabourie, A. J.; Köroğlu, Ç.; Pop, E. Substrate-Dependence of Monolayer MoS2 Thermal Conductivity and Thermal Boundary Conductance. *J. Appl. Phys.* **2022**, *131* (19), DOI: 10.1063/5.0089247.
(42) Zhang, L.; Lu, Z.; Song, Y.; Zhao, L.; Bhatia, B.; Bagnall, K. R.; Wang, E. N. Thermal Expansion Coefficient of Monolayer Molybdenum Disulfide Using Micro-Raman Spectroscopy. *Nano Lett.* **2019**, *19* (7), 4745−4751.
(43) Panasci, S. E.; Schilirò, E.; Greco, G.; Cannas, M.; Gelardi, F. M.; Agnello, S.; Roccaforte, F.; Giannazzo, F. Strain, Doping, and Electronic Transport of Large Area Monolayer MoS2 Exfoliated on Gold and Transferred to an Insulating Substrate. *ACS Appl. Mater. Interfaces* **2021**, *13* (26), 31248−31259.
(44) Rao, R.; Islam, A. E.; Singh, S.; Berry, R.; Kawakami, R. K.; Maruyama, B.; Katoch, J. Spectroscopic Evaluation of Charge-Transfer Doping and Strain in Graphene/MoS2 Heterostructures. *Phys. Rev. B* **2019**, *99* (19), No. 195401.
(45) Sahoo, S.; Gaur, A. P. S.; Ahmadi, M.; Guinel, M. J.-F.; Katiyar, R. S. Temperature-Dependent Raman Studies and Thermal Conductivity of Few-Layer MoS2. *J. Phys. Chem. C* **2013**, *117* (17), 9042−9047.
(46) Lanzillo, N. A.; Glen Birdwell, A.; Amani, M.; Crowne, F. J.; Shah, P. B.; Najmaei, S.; Liu, Z.; Ajayan, P. M.; Lou, J.; Dubey, M.; Nayak, S. K.; O'Regan, T. P. Temperature-Dependent Phonon Shifts in Monolayer MoS2. *Appl. Phys. Lett.* **2013**, *103* (9), DOI: 10.1063/1.4819337.
(47) Pop, E. The Role of Electrical and Thermal Contact Resistance for Joule Breakdown of Single-Wall Carbon Nanotubes. *Nanotechnology* **2008**, *19* (29), No. 295202.
(48) Liao, A. D.; Wu, J. Z.; Wang, X.; Tahy, K.; Jena, D.; Dai, H.; Pop, E. Thermally Limited Current Carrying Ability of Graphene Nanoribbons. *Phys. Rev. Lett.* **2011**, *106* (25), DOI: 10.1103/PhysRevLett.106.256801.
(49) Pop, E. Energy Dissipation and Transport in Nanoscale Devices. *Nano Res.* **2010**, *3* (3), 147−169.

https://doi.org/10.1021/acs.nanolett.5c05421
Nano Lett. XXXX, XXX, XXX−XXX